Journal of Nuclear Materials 378 (2008) 312–326

Contents lists available at ScienceDirect

Journal of Nuclear Materials

journal homepage: www.elsevier.com/locate/jnucmat

Strain-induced corrosion cracking behaviour of low-alloy steels under boiling water reactor conditions

H.P. Seifert *, S. Ritter

Paul Scherrer Institute (PSI), Nuclear Energy and Safety Research Department, Laboratory for Nuclear Materials, 5232 Villigen PSI, Switzerland

ARTICLE INFO

Article history:
Received 7 March 2008
Accepted 23 June 2008

ABSTRACT

The strain-induced corrosion cracking (SICC) behaviour of different low-alloy reactor pressure vessel (RPV) and piping steels and of a RPV weld filler/weld heat-affected zone (HAZ) material was characterized under simulated boiling water reactor (BWR)/normal water chemistry (NWC) conditions by slow rising load (SRL) and very low-frequency fatigue tests with pre-cracked fracture mechanics specimens. Under highly oxidizing BWR/NWC conditions (ECP $\geqslant$+50 mV$_{SHE}$, $\geqslant$0.4 ppm dissolved oxygen), the SICC crack growth rates were comparable for all materials (hardness <350 HV5) and increased (once initiated) with increasing loading rates and with increasing temperature with a possible maximum/plateau at 250 °C. A minimum K_I value of 25 MPa m$^{1/2}$ had to be exceeded to initiate SICC in SRL tests. Above this value, the SICC rates increased with increasing loading rate dK_I/dt, but were not dependent on the actual K_I values up to 60 MPa m$^{1/2}$. A maximum in SICC initiation susceptibility occurred at intermediate temperatures around 200–250 °C and at slow strain rates in all materials. In contrast to crack growth, the SICC initiation susceptibility was affected by environmental and material parameters within certain limits.

1. Introduction

Carbon (C) & low-alloy steels (LAS) are widely used for pressure boundary components such as piping and pressure vessels in fossil and nuclear light water reactors (LWR). Strain-induced corrosion cracking (SICC) in C & LAS de-aerators, feedwater piping and tanks, etc., continues to be the damage mechanism responsible for the largest percentage of availability loss in fossil power plants. Although SICC is less significant in LWR, it has occurred and is perceived to be a damage mechanism which needs to be considered for older plants, especially for those considering lifetime extension [1,2].

In case of C & LAS, SICC, which involves slow, dynamic straining with localized plastic deformation of material, but where obvious cyclic loading is absent, or restricted to a limited number of infrequent events such as plant start-up and shut-down, is increasingly used as an appropriate term to describe the area of overlap between stress corrosion cracking (SCC) under static and corrosion fatigue (CF) under cyclic loading conditions. The different types of environmentally-assisted cracking (EAC) and the currently available guidelines for evaluating and assessing EAC initiation and growth in C & LAS components in LWR are summarized in Table 1.

1.1. Service experience with SICC in LWR

The accumulated operating experience of C & LAS primary pressure boundary components in LWRs is very good worldwide. Isolated instances of EAC have occurred (particularly in boiling water reactor (BWR) service), most often in LAS piping and very rarely in the cladded reactor pressure vessel (RPV). EAC cracking has been observed in wrought, weld filler and weld heat-affected zone (HAZ) materials and has been transgranular in nature. In BWRs, steam and feedwater piping as well as condensate systems and RPV feedwater nozzles have been affected. In the secondary circuit of pressurized water reactors (PWR), cracking has been observed in feedwater piping/tanks and heat exchangers, feedwater nozzles of PWR steam generators and steam generator girth welds [1–7].

These EAC incidents have been clearly associated with an oxidizing environment (usually due to oxygen), severe dynamic straining (due to global and local thermal stratification/striping or due to thermal and pressurization cycles during plant transients), and high local stresses around or above the high-temperature yield strength or high secondary/residual stress (due to, e.g., welding defects, pipe bends in conjunction with inadequate pipe support or restraints, localized post-weld treatment). Corrosion during shut-down periods (e.g., pitting) was sometimes a further contributing factor. Thermal-hydraulics (thermal stratification/striping phenomena) and local stress raisers played a key role and were usually more important than water chemistry or material aspects. These cases were attributed either to SICC or CF. Cracking

---

* Corresponding author. Tel.: +41 56 310 44 02; fax: +41 56 310 21 99.
E-mail address: hans-peter.seifert@psi.ch (H.P. Seifert).

0022-3115/$ - see front matter © 2008 Elsevier B.V. All rights reserved.
doi:10.1016/j.jnucmat.2008.06.035

Table 1
Basic types of EAC in C & LAS and relevant nuclear codes

Mechanism	Environmentally-assisted cracking (EAC)		
	SCC Stress corrosion cracking	SICC Strain-induced corrosion cracking	CF Corrosion fatigue
Type of loading	Static	Slow monotonically rising or very low-cycle	Cyclic: low-cycle, high-cycle
LWR operation condition	Transient-free, steady-state power operation	Start-up/shut-down, thermal stratification	Thermal fatigue, thermal stratification, etc.
Characterization of crack growth	BWRVIP-60 disposition lines	?	ASME XI, Code Case N-643 (PWR)
Characterization of crack initiation	? (σ > YS)	Susceptibility conditions: $\mathrm{ECP}_{\mathrm{crit}}$, $\mathrm{d}\varepsilon/\mathrm{d}t_{\mathrm{crit}}$, $\varepsilon_{\mathrm{crit}}$	ASME III, F_{env}-approach

incidents with a major or relevant contribution of SCC to the total crack advance in properly manufactured and heat-treated low-alloy primary pressure boundary components were not observed [1–7].

1.2. SICC susceptibility conditions

The SICC behaviour of C & LAS was mainly characterized by slow strain rate (SSR) [7–15] and low-cycle fatigue (LCF) tests [7,16–19] with smooth specimens. Based on these tests, critical system conditions for the occurrence of SICC could be established.

SICC (and significant environmental reduction of LCF lives) may occur in C & LAS in oxygenated, high-purity high-temperature water, if the following conditions are simultaneously attained:

- Corrosion potential $\mathrm{ECP} > \mathrm{ECP}_{\mathrm{crit}} = -200\ \mathrm{mV}_{\mathrm{SHE}}$.
- Strain rate in a critical range: $0 < \mathrm{d}\varepsilon/\mathrm{d}t_{\mathrm{crit,\ min}} \leqslant \mathrm{d}\varepsilon/\mathrm{d}t \leqslant \mathrm{d}\varepsilon/\mathrm{d}t_{\mathrm{crit,max}} = 10^{-3}\ \mathrm{s}^{-1}$.
- (Local) macroscopic strain above the elastic limit: $\varepsilon \geqslant \varepsilon_{\mathrm{crit}} = 0.1\%$.
- Temperature $T > 150$ °C.
- Sulphur content >0.003 wt% S.

If one of these conjoint threshold conditions is not satisfied, SICC initiation is extremely unlikely and no or only minor environmental reduction of LCF life is observed in high-temperature water. Sulphate and chloride may shift the susceptibility region to less severe conditions (e.g., lower ECP and strains) [1].

1.3. Objectives of this work

Service experience has thus clearly shown that SICC may occur in C & LAS pressure boundary components in LWRs under unfavourable conditions [1–7]. Furthermore, laboratory background knowledge [1,6,16–20] indicates, that the current 'ASME III fatigue design' and 'ASME XI fatigue crack growth evaluation curves' in Sections III and XI of the ASME Boiler and Pressure Vessel Code might be non-conservative for certain ranges of these critical system conditions.

In contrast to the SICC and LCF initiation behaviour, there is a relevant lack of reliable quantitative information on the SICC and low-frequency corrosion fatigue (LFCF) crack growth behaviour under these critical conditions. Normal SSR and LCF tests involve nominal strains in the plastic range and plastic yielding of the un-cracked ligament. Thus, although these types of tests contain information on SICC crack growth, the results may not be transferable to fully constrained deep cracks in pressure boundary components with small scale yielding (linear-elastic fracture mechanics behaviour). Therefore, the SICC and LFCF behaviour of different low-alloy RPV steels was investigated by slow rising load (SRL) and low-frequency fatigue tests with pre-cracked specimens under these critical conditions within several research projects at Paul Scherrer Institute (PSI).

The present paper is a summary of the SRL results. The LFCF behaviour is discussed in detail in a separate paper [20]. After a brief introduction of the applied experimental procedure (Section 2), the most important mechanical loading, environmental and material parameter effects on SICC crack growth are summarized in Section 3 and compared to SSR test results. The SICC behaviour in SRL experiments is then compared to low and very low-frequency CF test results in Section 4. Thereafter, the basic local control factors for SICC crack growth are derived and discussed in Section 5. Finally, the experimental observations are compared to service experience in Section 6.

2. Materials and experimental procedure

The SICC crack growth behaviour of different RPV materials was characterized by SRL and LFCF tests with pre-cracked fracture mechanics specimens. The tests were performed in modern high-temperature water loops (Fig. 1) under simulated stationary and transient BWR/NWC conditions, i.e. in oxygenated high-temperature water at temperatures of either 288, 250, 200 or 150 °C under low-flow conditions (4–5 autoclave exchanges per hour) with local flow rates of some few mm/s. The dissolved oxygen (DO) and sulphate concentration of the environment were varied from <0.005 to 8 ppm and <1 ppb (high-purity water) to 365 ppb, respectively. In most tests a DO content of 0.4 or 8 ppm was applied. A DO of 0.4 ppm represents the total oxidant concentration in the reactor water during steady-state power operation in a realistic way. The increased DO value of 8 ppm was applied additionally to either simulate plant transients (e.g., start-up) and locations with oxygen enrichment (e.g., piping with stagnant steam or non-degassed condensate) or to achieve a realistic ECP of $+150\ \mathrm{mV}_{\mathrm{SHE}}$ for a surface crack penetrating the stainless steel cladding on the RPV wall/nozzles. These conditions may appear to be overly aggressive/conservative for many other LAS BWR pressure boundary components (e.g., feedwater piping or piping with flowing steam).

2.1. Materials and specimens

Several different types of low-alloy RPV steels (base metal and HAZ) and a RPV weld filler material were investigated (Tables 2–4). The investigated materials are characteristic for RPV of Western LWR. Concerning the EAC behaviour, the steels mainly differed in their DSA susceptibility and sulphur content/MnS morphology.

All base materials were quenched and tempered. The weld filler, weld HAZ, and some base materials were post-weld heat-treated or stress relieved. The RPV steels had a granular, bainitic (alloy A, C, D, and F) or a mixed bainitic/ferritic-pearlitic structure (alloy B) with an average former austenitic grain size of 10–20 μm. The spatial distribution and morphology of the MnS inclusions was

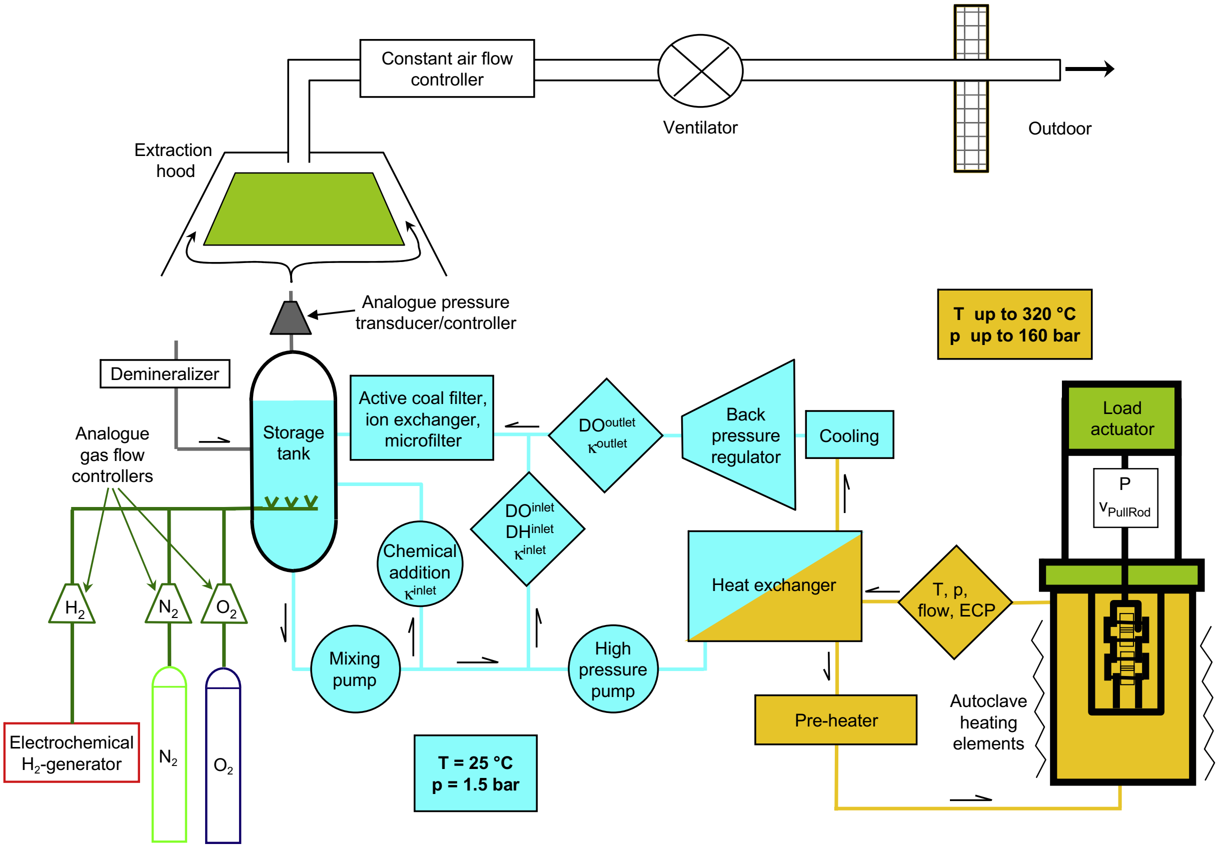

Fig. 1. Schematic of high-temperature water loop with autoclave and electro-mechanical tensile machine.

Table 2
Overview of investigated low-alloy RPV steels

Material		S (wt%)	Al (wt%)	N_{free} (ppm)	Heat treatment	Micro structure	$R_P^{288\ °C}$ (MPa)	DSA-index
20 MnMoNi 5 5 (≡ SA 508 Cl.3)	A	0.004	0.013	30	910–920 °C/6 h/WQ, 640-650 °C/9.5 h/FC	Bainitic	418	−12.3% +++
SA 508 Cl.2 (≡ 22 NiMoCr 3 7)	B	0.004	0.015	2	900 °C/ 8 h/WQ, 600 °C/9 h/AC	Bainitic/ferritic-pearlitic	396	−16.4% +++
SA 533 B Cl.1 (≡ 20 MnMoNi 5 5)	C	0.018	0.030	<1	915 °C/12 h/AC/860 °C/12 h/WQ 660 °C/12 h/FC/610 °C/40 h/FC 550 °C/12 h/FC/550 °C/12 h/FC	Bainitic	412	−8.9% ++
22 NiMoCr 3 7 (≡ SA 508 Cl.2)	D	0.007	0.018	3	890–900 °C/7 h/WQ 640-650 °C/17 h/AC +SR (see Material E)	Bainitic	400	−0.58% +
S3 NiMo 1 (RPV weld filler)	E	0.007	0.005	16	SR: 540–555 °C/59 h/465 °C/590–610 °C/21 h/ 465 °C/ 590-605 °C/11.25 h/AC	Ferritic	430	−2.6% +
20 MnMoNi 5 5 (≡ SA 508 Cl. 3)	F	0.015 (0.003–0.053)[a]	0.029	nm	900 °C/9 h/WQ/650 °C/34 h/AC/660 °C/14 h/ AC/550 °C/47 h/600 °C/8 h/AC	Bainitic	439	−9.1% ++
Weld HAZ of D	G	0.007	0.018	nm	540–555 °C/59 h/465 °C/ 590- 610 °C/21 h/ 465 °C/ 590–605 °C/11.25 h/AC	–	640	nm

R_P = yield strength, WQ = water quenched, FC = furnace cooled, AC = air cooled, SR = stress relief heat treatment, nm = not measured, DSA-index (T = 250 °C) = $(Z_{1E-3\%/s} - Z_{1E-1\%/s})/Z_{1E-1\%/s}$ = ductility loss, +++: high, ++: medium, +: low DSA susceptibility.

[a] Steel with relevant sulphur segregation → range of results of sulphur measurements at different locations.

Table 3
Chemical composition in wt% of investigated RPV steels and weld filler materials

Material		C	Si	Mn	P	S	Cr	Mo	Ni	V	Al	Cu
20 MnMoNi 5 5	A	0.21	0.25	1.26	0.004	0.004	0.15	0.5	0.77	0.008	0.013	0.06
SA 508 Cl. 2	B	0.21	0.27	0.69	0.005	0.004	0.38	0.63	0.78	0.006	0.015	0.16
SA 533 B Cl. 1	C	0.25	0.24	1.42	0.006	0.018	0.12	0.54	0.62	0.007	0.03	0.15
22 NiMoCr 3 7	D	0.215	0.20	0.91	0.008	0.007	0.42	0.53	0.88	0.007	0.018	0.04
S3 NiMo 1 Weld Filler	E	0.054	0.17	1.19	0.013	0.007	0.04	0.55	0.94	0.006	0.0053	0.06
20 MnMoNi 5 5	F	0.26	0.32	1.44	0.016	0.015	0.15	0.61	0.63	0.02	0.029	0.17
Weld HAZ of G	G	0.215	0.20	0.91	0.008	0.007	0.42	0.53	0.88	0.007	0.018	0.04

Table 4
Mechanical tensile test properties of investigated RPV steels and weld materials

Material		25 °C				288 °C
		$R_{P_{0.2}}$ (MPa)	R_m (MPa)	A_5 (%)	Z (%)	$R_{P_{0.2}}$ (MPa)
20 MnMoNi 5 5	A	485	648	19.3	72.1	418
SA 508 Cl. 2	B	448	611	17.9	71.0	396
SA 533 B Cl. 1	C	456	605	23.4	59.9	412
22 NiMoCr 3 7	D	467	600	17.3	71.9	400
S3 NiMo 1 Weld Filler	E	492	592	17.4	73.3	430
20 MnMoNi 5 5	F	508	664	20	61	439
Weld HAZ of D	G	640*	–	–	–	–

($R_{P0.2}$: Yield strength, R_m: Ultimate tensile strength, A_5: Uniform elongation, Z: Reduction of area, * = with instrumented hardness tester).

fairly homogeneous and similar in alloys A–D covering the range from small, spherical to large (up to a few 100 µm), elongated inclusions. Alloy F revealed distinct banded sulphur segregation zones with large clusters of MnS inclusions. The weld filler material E had a very fine-grained, ferritic microstructure with a mean grain size of ⩽6 µm. This material revealed a very fine-dispersed distribution of extremely small (⩽1 µm), spherical MnS-inclusions. The maximum microhardness and tensile residual stress in the region of the HAZ G was limited to 350 HV 0.5 and to 30–40 MPa.

Twenty five millimetre thick compact tension specimens (1T–C(T)) according to ASTM E399 were used for all experiments. The base metal specimens were manufactured from forged ingots or hot-rolled steel plates mainly in T–L or L–T orientation. The weld metal and weld HAZ specimens were manufactured in the T–L or L–T and T–S or T–L orientation. The specimens were pre-cracked by fatigue in air at room temperature, using a load ratio R of 0.1. The maximal K_I at the final load step was ⩽15 MPa m$^{1/2}$. The fatigue pre-crack of the HAZ specimens was positioned in the middle of the HAZ close to the peak hardness region.

2.2. Experimental procedure

2.2.1. Experimental facilities

The SICC tests were performed in 10 l stainless steel autoclaves with integrated electromechanical loading systems, which were attached to sophisticated refreshing high-temperature water loops (Fig. 1). Usually, two air fatigue pre-cracked, 25 mm thick 1T C(T) were tested simultaneously in a serial chain. The crack mouth opening displacement CMOD_{LL} of both specimens was measured by clip gauges. During the experiments all important mechanical loading (load, CMOD_{LL}, pull rod stroke, etc.) and environmental parameters at inlet and outlet (DO, DH, κ, T, p, flow, etc.) were recorded continuously. The electrochemical corrosion potential (ECP) of the specimens and the redox potential (platinum probe) were continuously monitored by use of an external Ag/AgCl/0.01 M KCl- or a $Cu/Cu_2O/ZrO_2$-membrane reference electrode. Ionic impurities of the water (inlet and outlet) were analyzed by Inductively Coupled Plasma–Atomic Emission Spectroscopy (ICP–AES) and Ion Chromatography (IC) about four times each test. The specimens were electrically insulated from the autoclave, from each other, and from the clip gauges by ZrO_2 spacers. The ECP reached a quasi steady-state during the conditioning phase and only rose about 10–30 mV during the test phase. In Fig. 2 the quasi-stationary ECPs as a function of DO at 288 °C and as a function of temperature at a DO of 8 ppm and 0.4 ppm are shown.

2.2.2. Crack length monitoring

Crack advance was continuously monitored using the reversed direct current potential drop (DCPD) method. The crack growth increment was calculated by the Johnson formula. The mean pre-fatigue crack length $\langle a_0 \rangle$ was assigned to the potential drop at the point of crack growth initiation during initial loading in the test, as determined according to ASTM E 1737 (Fig. 3). The calculated crack length at the end of the experiment was then verified and, if necessary, corrected with regard to the mean final crack length $\langle a_0 + \Delta a_{\text{SICC}} \rangle$ as revealed by post-test fractography. In the case of fairly uniform SICC crack advance, the difference between calculated and fractographically determined increment of crack advance was <5%. The evaluated DCPD resolution limit corresponded to roughly 2–5 µm (depending on test conditions).

The specimens were broken apart at liquid nitrogen temperature for post-test evaluation. For fractographical analysis in the SEM, the oxide film on the fracture surface of one specimen half was removed by galvanostatic reduction in an ENDOX-bath [23].

The K_I values were calculated according to ASTM E 399 by the measured load and by the actual mean crack length $a_0 + \Delta a_{\text{SICC}}$, derived by post-test fractographical evaluation and the DCPD method.

2.2.3. Test procedure

The different phases of the experiments are shown in Fig. 4. The specimens were loaded with a small mechanical pre-load of

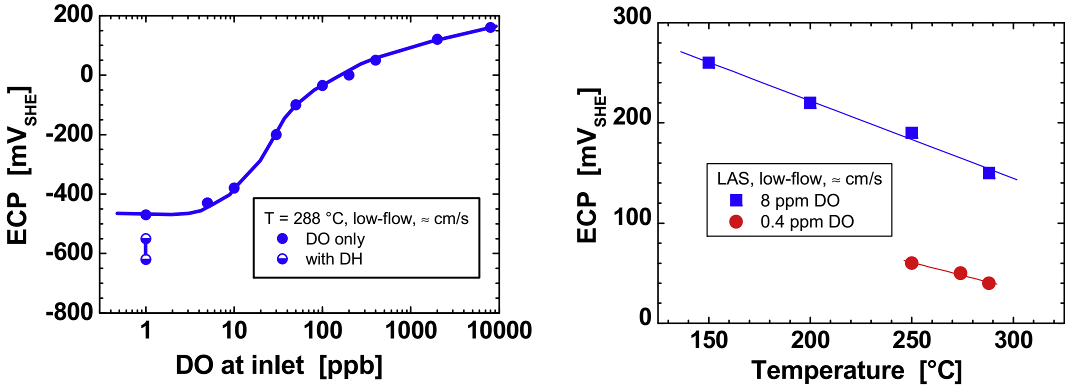

Fig. 2. Effect of DO (left plot) and temperature (right plot) on ECP of LAS.

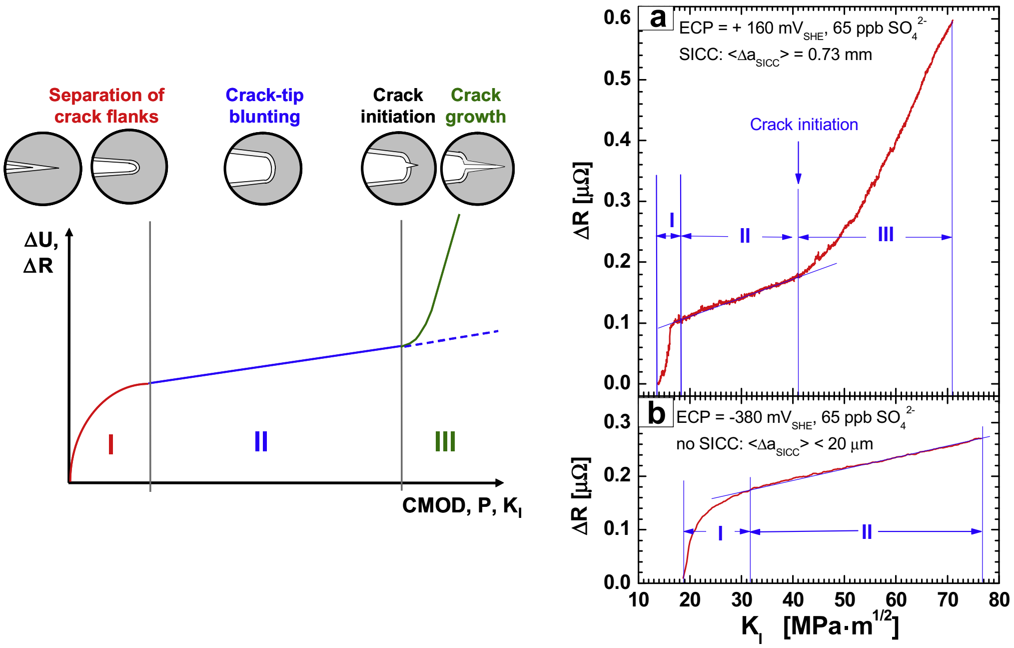

Fig. 3. Left plot: Schematic of DCPD signal (potential & resistance drop ΔU & ΔR) during SRL tests. Transition from region II to region III corresponds to point of crack initiation. Right plot: DCPD signal during SRL tests: (a) SICC initiation & growth at 8 ppm DO. (b) No SICC initation at <0.005 ppm DO.

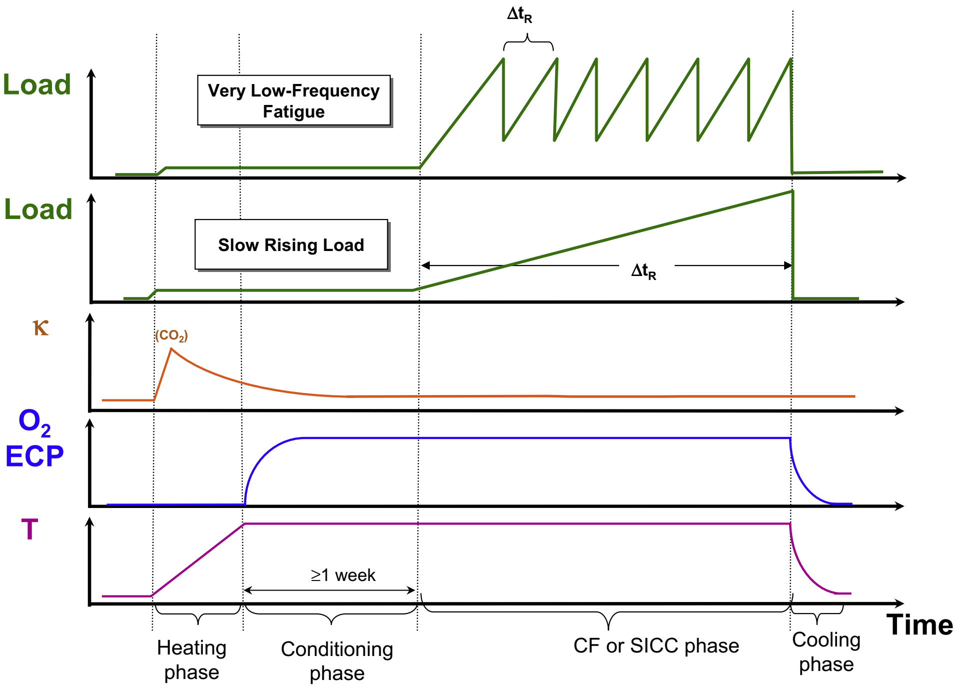

Fig. 4. Schematic of applied test procedure in SRL and LFCF experiments.

approximately 9 kN, corresponding to a K_I between 12 and 18 MPa m$^{1/2}$, and the autoclave was heated in deoxygenated high-purity water. Thereupon the conditioning phase followed, where the environmental parameters were adjusted and the specimens were pre-oxidized for $\geqslant 168$ h. In the core test phase, the loading of the specimens in SRL tests and the initial loading in LFCF tests were performed by using a constant rate of the pull rod stroke ($\approx$ constant dP/dt, $dCOD/dt$ and dK_I/dt values). The subsequent cyclic loading in the very low-frequency CF tests was performed under load control. Constant load amplitude loading with a positive saw tooth waveform (slow loading, fast unloading) was applied. Finally, the specimens were unloaded and the autoclave cooled down.

3. Major parameter effects on SICC initiation and growth

3.1. Effect of loading rate and level

The effect of loading rate on SICC initiation and subsequent growth was systematically studied in RPV materials A, B, and C at a temperature of 288 °C. The tests were conducted with a DO of 8 ppm (ECP = +150 mV$_{SHE}$) and an inlet conductivity of 0.25 µS/cm (65 ppb SO_4^{2-}). In Fig. 5 the crack growth initiation stress intensity factor $K_{I,i}$ and SICC growth rate da/dt_{SICC} are plotted versus the displacement rate at the load line $dCOD_{LL}/dt$ and stress intensity factor rate dK_I/dt for the high-sulphur steel C. The high-sulphur steel C (0.018 wt% S) revealed SICC over the whole range of tested loading rates. In this material, $K_{I,i}$ decreased with decreasing loading rate, with a possible minimum of 34 MPa m$^{1/2}$ at a relatively low displacement rate of ≈10^{-6} mm/s, corresponding to an estimated crack-tip strain rate of $5 \cdot 10^{-5}$ to 10^{-4} s^{-1}. At lower loading rates, $K_{I,i}$ seemed to increase again. The subsequent SICC crack growth rate (CGR) was constant during the whole rising load phase after a short transition period following SICC initiation. The SICC CGR depended strongly on the applied loading rate, but not on the actual value of K_I, at least up to a K_I of 60–70 MPa m$^{1/2}$. Here, a simple power law relationship with an exponent of 0.8 was found between SICC CGR and $dCOD_{LL}/dt$ and dK_I/dt (Fig. 5). Thus, both SICC initiation and growth were strongly dependent on the applied loading rate, but with opposite tendency. The observed high SICC CGR of 10^{-9} m/s (0.1 mm/day) to $8 \cdot 10^{-7}$ m/s (70 mm/day) could only be perceived if initiation occurred. This requires high stress intensities, which would correspond to relatively deep cracks in the pressure boundary components.

In alloys A and B with a low sulphur content of 0.004 wt%, SICC could only be detected by DCPD at the lowest loading rates applied ($2\text{–}3 \cdot 10^{-7}$ mm/s and $3 \cdot 10^{-6}$ mm/s). The measured SICC growth rates were within the scatter range of the results of high-sulphur alloy C, whereas the $K_{I,i}$ values were slightly (for $dCOD_{LL}/dt = 2\text{–}3 \cdot 10^{-7}$ mm/s) or significantly (for $dCOD_{LL}/dt = 2\text{–}4 \cdot 10^{-6}$ mm/s) higher. At higher loading rates, the extent of SICC revealed by fractography was restricted to some few very localized thumbnail-shaped areas along the former pre-crack front. The mean crack increment was well below the DCPD resolution limit of ≈5 µm. The beneficial effect of a low sulphur content on SICC initiation disappeared at very slow loading rates, which might be related to the increased DSA susceptibility of these two steels with respect to the high-sulphur alloy C (see Section 3.3.2).

3.2. Effect of environmental parameters

3.2.1. ECP and DO

The effect of ECP and DO was investigated in RPV materials A, and C at a temperature of 288 °C in the loading rate range of maximum SICC susceptibility ($dCOD_{LL}/dt = 2\text{–}4 \cdot 10^{-6}$ mm/s). The different ECPs were set by different DO contents of <0.005, 0.2 and 8 ppm in high-temperature water with 65 ppb SO_4^{2-}.

For these loading rate and temperature conditions, SICC could only be detected by DCPD in experiments with the high-sulphur steel C in high-temperature water with the highest DO content of 8 ppm. At a DO level of 0.2 ppm, few thumbnail-shaped regions with minor SICC crack growth were observed along the pre-crack front in both materials by post-test fractography in the SEM. This local SICC often originated from MnS-inclusions, which intersected the pre-crack front, but not exclusively. The maximum local SICC crack advance in the high-sulphur steel C at 0.2 ppm DO was similar to that of the low-sulphur alloy A at the higher DO content of 8 ppm. In deoxygenated water (<0.005 ppm DO), no SICC was observed by post-test fractography in all three materials up to very high stress intensity factors of up to 76 MPa m$^{1/2}$. This indicates a critical cracking potential ECP$_{crit}$ for SICC in SRL tests under these conditions of −100 to −200 mV$_{SHE}$, which reasonably correlates with ECP$_{crit}$ derived from SSR experiments with smooth tensile specimens [9–11].

The strong effect of ECP or DO on SICC initiation (and subsequent crack growth) is exemplarily shown in Fig. 6 for the high-sulphur steel C. Here, the maximum local SICC advance derived by post-test fractography in specimens from SRL tests with a displacement rate $dCOD_{LL}/dt$ of $2\text{–}4 \cdot 10^{-6}$ mm/s, which were loaded up to the same maximum stress intensity factor K_I^{max} of approxi-

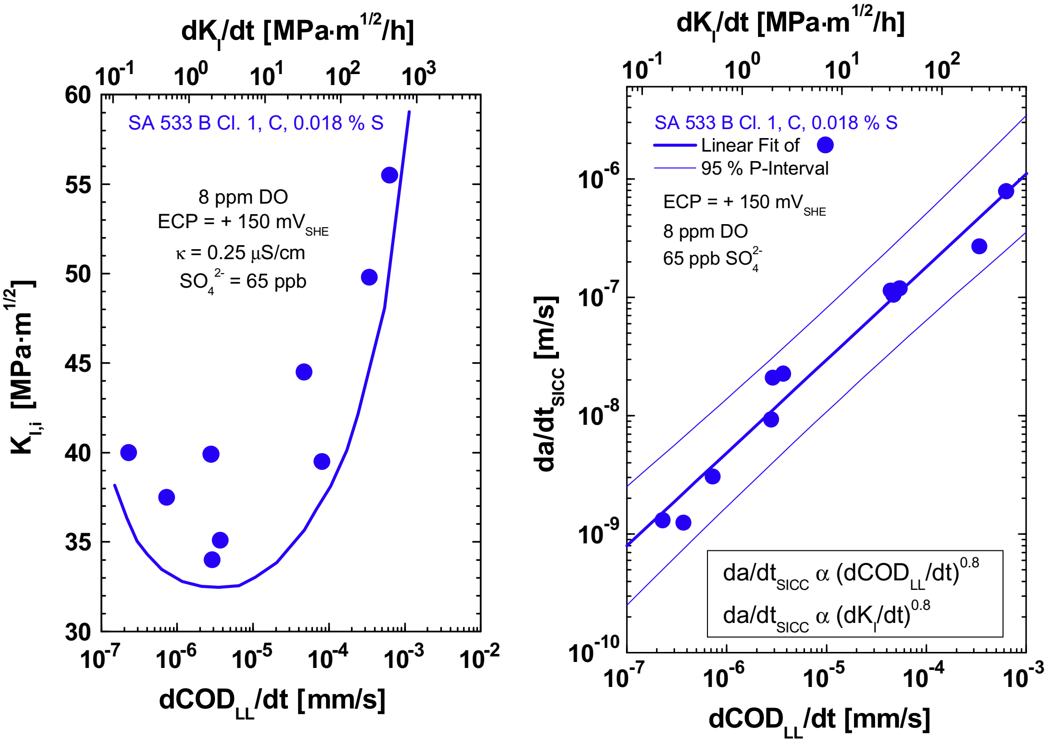

Fig. 5. Effect of loading rate on SICC initiation (left plot) and crack growth (right plot) in high-sulphur steel C.

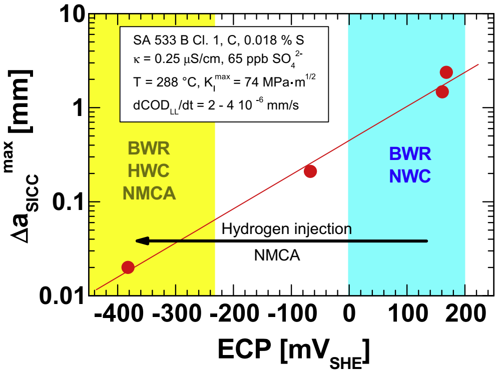

Fig. 6. Effect of ECP on local maximum SICC crack advance in SRL experiments under identical loading conditions.

mately 74 MPa $m^{1/2}$, is plotted versus the corrosion potential ECP. From Fig. 6 it is evident that SICC susceptibility can be significantly reduced by the reduction of the ECP through, e.g., hydrogen water chemistry (HWC) or HWC in combination with noble metal chemical addition (NMCA). Under PWR conditions, this ECP_{crit} threshold is usually only exceeded under some very specific operational conditions, or at special locations, where (temporary) increased DO levels cannot be fully excluded or avoided.

3.2.2. Sulphate

The effect of sulphate was investigated in the concentration range from <1 ppb (<0.06 µS/cm) to 365 ppb (1.0 µS/cm) in SRL experiments at a displacement rate $dCOD_{LL}/dt$ of 2–4·10^{-6} mm/s in high-temperature water at 288 °C with a DO content of 8 ppm (+150 mV_{SHE}).

In the high-sulphur steel C, neither the SICC initiation stress intensity factors $K_{I,i}$ nor the SICC growth rate da/dt_{SICC} were affected by the addition of sulphate and comparable values were observed for all sulphate levels. In the low-sulphur alloy A SICC was restricted to some few localized regions along the pre-crack front at sulphate levels ⩽65 ppb, which could not be detected by DCPD. At a sulphate level of 365 ppb on the other hand, SICC extended over almost the whole crack front. Here, the SICC growth rates in the low-sulphur alloy A was within the scatter band for the high-sulphur steel C (Figs. 7a and 7b), whereas their SICC initiation stress intensity factors $K_{I,i}$ were slightly higher.

As shown in Figs. 7a and 7b, the addition of a sufficient amount of sulphate can result in a similar SICC susceptibility in low-sulphur steels as in high-sulphur materials. The results from materials and environments with different steel sulphur contents and sulphate/DO concentrations (Figs. 7a and 7b), indicate that a critical sulphur anion threshold in the crack-tip electrolyte has to be exceeded for a high SICC cracking susceptibility (see also Section 5). This threshold and SICC are thus synergistically controlled by material (sulphur) and environmental parameters (ECP and sulphate concentration). If this threshold concentration is exceeded, the SICC growth rate only increases with increasing loading rate, but neither depends on the steel sulphur content nor change by further increasing the sulphate content of the environment (Fig. 7a).Therefore, it does not matter, whether the sulphur anions originate from the dissolution of the MnS-inclusions, which are intersected by the crack flanks and front, or from the presence of sulphate as an impurity in the bulk environment outside the crack.

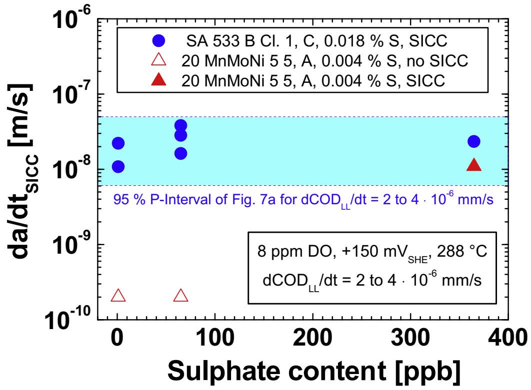

Fig. 7b. Effect of sulphate concentration on SICC crack growth in oxygenated high-temperature water in the low- and high-sulphur steel A and C at a loading rate $dCMOD_{LL}/dt$ of 2–4·10^{-6} mm/s.

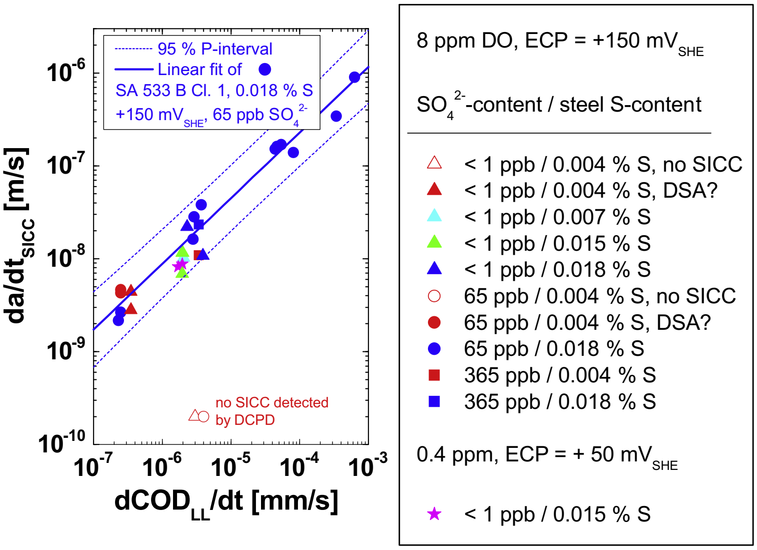

Fig. 7a. Effect of sulphate concentration and steel sulphur content on SICC crack growth in oxygenated high-temperature water, which indicates the existence of a critical sulphur anion concentration in crack-tip electrolyte for SICC.

Besides the reduction of the ECP or DO level (e.g., HWC, evacuation), also a high purity of the feed and reactor water as well as the selection of optimized materials with low sulphur contents (and low DSA susceptibilities) contribute to a reduced SICC susceptibility.

3.2.3. Temperature

Tests at temperatures of 150, 200, 250 and 288 °C with the low-sulphur steels A and B and with the high-sulphur steel C, as well as with the weld filler and HAZ materials E and G were performed in oxygenated high-temperature water (DO = 8 ppm) with a SO$_4^{2-}$ content of 65 ppb. The ECP decreased slightly from +250 mV$_{SHE}$ at 150 °C to +130 mV$_{SHE}$ at 288 °C. A displacement rate of 4·10^{-6} mm/s in the range of maximal SICC susceptibility at 288 °C was used for these tests. The effect of temperature on SICC initiation and growth is exemplarily shown in Fig. 8 for the weld filler material E. The results of the different materials are compared in Fig. 9. At 288 °C, SICC could be detected by DCPD in all steels, except the low-sulphur alloy A. The lowest $K_{I,i}$ values were observed in HAZ G, followed by the high-sulphur alloy C and the medium- and low-sulphur weld filler alloy E and base material B. The SICC growth rate was slightly higher in the high-sulphur alloy C than in the other alloys. At 250 °C, SICC was observed in all alloys, with comparable $K_{I,i}$ values and SICC growth rates. At 200 and 150 °C, surprisingly, only the high-sulphur alloy C revealed no SICC by DCPD. For the chosen loading rate, a minimum in $K_{I,i}$ values and a maximum in SICC susceptibility was observed at intermediate temperatures around 200–250 °C for all materials, whereas the SICC CGRs increased slightly with increasing temperature with a possible maximum/plateau at/above 250 °C. In the temperature range from 150 to 250 °C, an Arrhenius activation energy E_A of 32 ± 3 KJ/mol was calculated, which correlated well with corresponding values for CF [20] and SCC crack growth [24] under comparable conditions. If SICC crack growth could be detected by DCPD, SICC CGRs were similar for all five materials (Fig. 9). The lower SICC susceptibility of the high-sulphur alloy C at the lower temperatures of 150 and 200 °C, which was further confirmed by SCC tests under constant load, is initially surprising and shows that the steel sulphur content is not the sole material parameter strongly affecting the SICC susceptibility of LAS.

The susceptibility of the examined alloys to DSA might be a possible reason for the maximum in SICC susceptibility at intermediate temperatures (200–250 °C) and for the SICC susceptibility of the low-sulphur alloys A and B at very slow strain rates at 288 °C (see also Section 3.3.2). This was clearly supported by the good correlation in terms of temperature between the maximum in susceptibility to SICC (minimum of $K_{I,i}$) of RPV steels in SRL tests under oxygenated high-temperature water conditions and the maximum in DSA susceptibility (minimum in reduction of area) in tensile tests in air at comparable strain rates was observed (see Fig. 10).

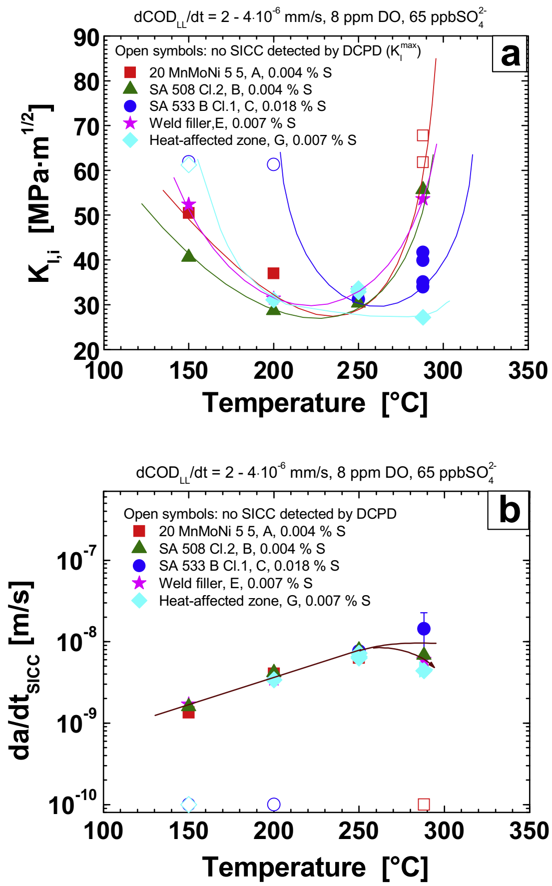

Fig. 9. Effect of temperature on SICC initiation (a) and crack growth; (b) for various alloys.

3.3. Effect of material parameters

3.3.1. Steel sulphur content and MnS-morphology

Besides the sulphur content of the steel, the size, type (chemical composition), shape and spatial distribution of MnS-inclusions

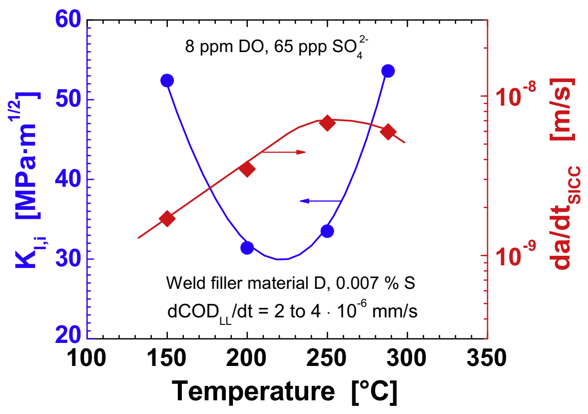

Fig. 8. Effect of temperature on SICC initiation and growth in weld filler metal E.

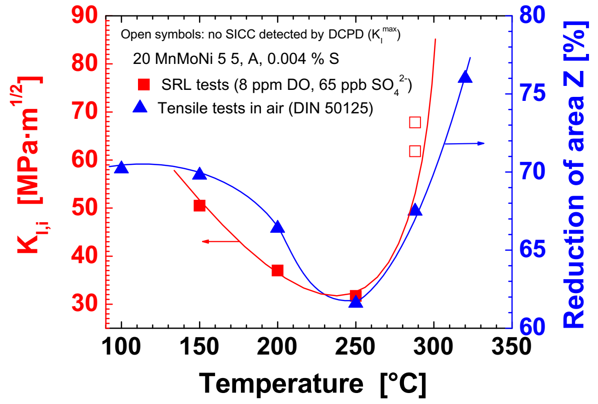

Fig. 10. Comparison of $K_{I,i}$ values of SRL experiments with reduction of area values of tensile tests in air at comparable strain rates in alloy A. A good correlation between maximum in SICC and DSA susceptibility in terms of temperature is observed.

may have an effect on EAC in C & LAS. The local sulphur content and morphology of MnS-inclusions depend on the steel making (→ segregation) and fabrication process of the plate (forming: hot rolling, forging, etc.) and they can significantly differ in large plates. The concentration of sulphides is generally higher in the centre of the plate. In segregation zones the local sulphur content can be several times larger than the mean bulk sulphur content. Sulphides tend to be rod-like in unidirectionally-rolled plates, and disk-like in cross-rolled plates, while in forgings and weld metals the sulphides tend to be more spherical. The orientation of the crack planes in specimens (T–L, L–T, T–S, etc.) and the location of specimens in plates and forgings might therefore affect the SICC behaviour.

A distinct effect of specimen orientation (T–L, L–T, and T–S) or location (0T, 1/4T, 1/2T, 3/4T, and 1T) was not observed in the PSI investigations. The SICC CGRs were comparable for all orientations (Fig. 11) and locations. This may be related to the homogeneous sulphur distribution in all alloys (except steel F) and the high corrosion potential of +150 mV_{SHE} which favours the enrichment of sulphides in the crack enclave by potential-gradient-driven migration [4,25].

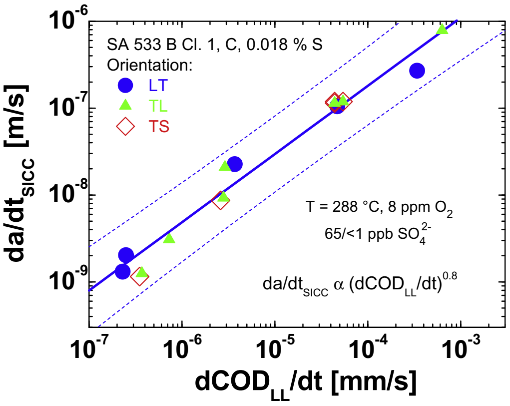

Fig. 11. Similar SICC growth rates in high-sulphur steel C for different specimen orientations.

In oxygenated high-temperature water (0.4–8 ppm DO) of moderate purity ($\leqslant$65 ppb SO_4^{2-}) at 288 °C a beneficial effect of a low steel sulphur content on the SICC susceptibility was observed under some loading rate conditions. In alloys with low and medium sulphur contents higher stress intensity factors $K_{I,i}$ were required to initiate SICC in SRL tests than in high-sulphur steels (Figs. 9, 12 and 13). On the other hand, the steel sulphur content and specimen orientation had very little effect on SICC growth rates (Figs. 7, 9, 11, 12, and 13). This could be explained by large, elongated MnS-inclusions, which are intersected by the pre-crack front and which may act as preferential initiation sites for EAC. The higher $K_{I,i}$ values in the low-sulphur alloy A and B and in the medium-sulphur weld material D might be attributed to the fact that less large MnS-inclusions were intersected by the pre-crack front in these materials, resulting in a lower probability for crack initiation or in an initially more localized non-uniform crack growth.

The beneficial effect of a low steel sulphur content on SICC susceptibility at temperatures >250 °C and sulphate concentrations $\leqslant$65 ppb can be completely overwhelmed by the selection of suitable combinations of the corrosion potential ECP (or DO) and sulphate content of the environment (Figs. 7a and 7b) and/or of temperature (Figs. 9 and 13) and loading rate (Fig. 12).

3.3.2. Dynamic strain ageing

At low temperatures of 150 and 200 °C the low-sulphur steels A and B and the medium-sulphur weld filler material E revealed a higher SICC susceptibility than the high-sulphur alloy C (Fig. 9). Furthermore, in high-purity water (<1 ppb SO_4^{2-}) with 8 ppm DO the low-sulphur steels A and B revealed a comparable SICC susceptibility at very low loading rates $dCOD_{LL}/dt = 2–3 \cdot 10^{-7}$ mm/s as the

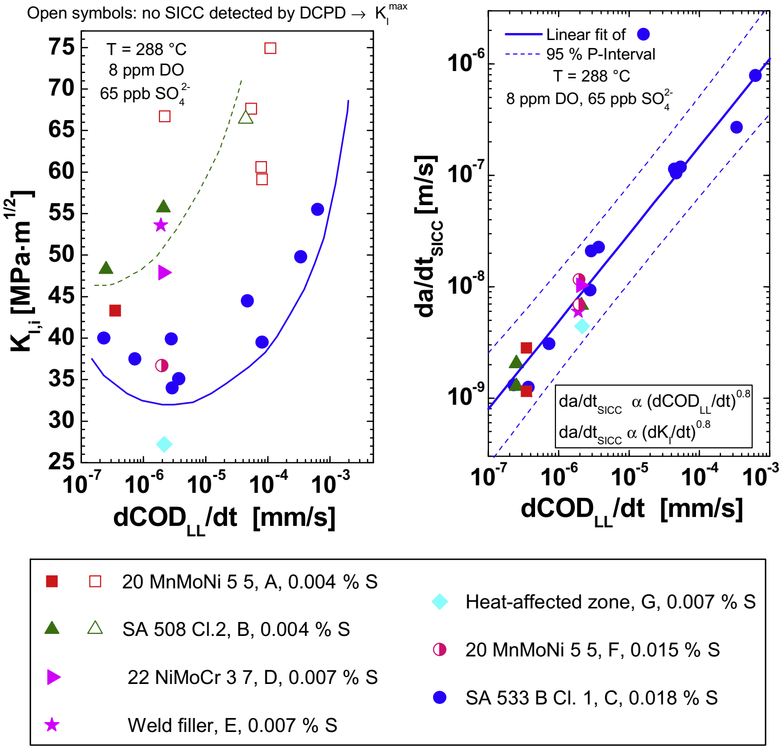

Fig. 12. Comparison of SICC initiation susceptibility (left plot) and SICC growth rates in various LAS with different steel sulphur contents at 288 °C.

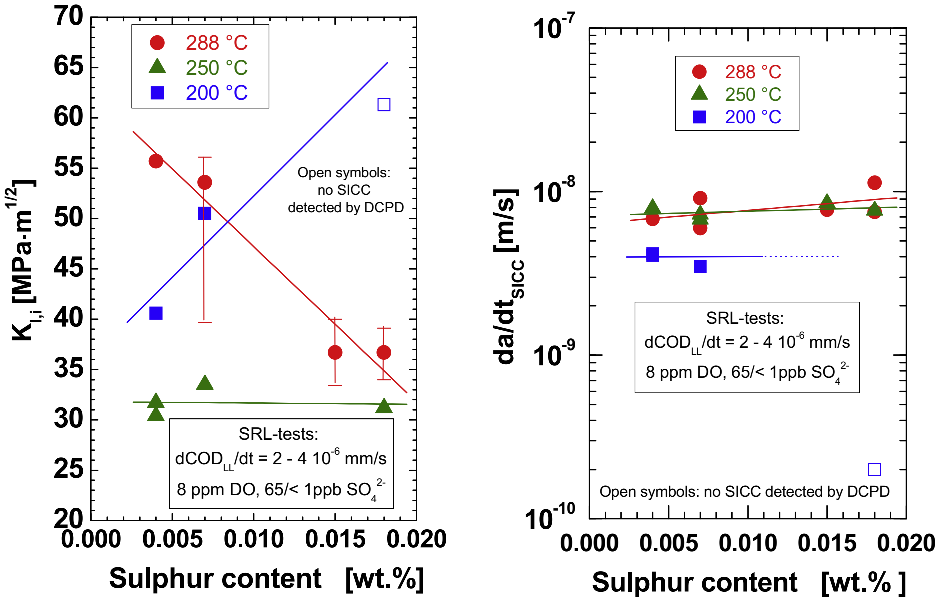

Fig. 13. Effect of steel sulphur content on SICC initiation (left plot) and crack growth (right plot) in various LAS at different temperatures.

high-sulphur alloy C. These results together with the peak of SICC susceptibility at intermediate temperatures indicate, that under certain temperature–strain rate combinations DSA might significantly affect the EAC behaviour in susceptible LAS.

The DSA susceptibility of the various alloys in tensile tests at different temperatures and strain rates and in internal friction experiments correlated reasonably well with the temperature and strain rate dependence of the SICC susceptibility, and in particular with the SCC growth rates at intermediate temperatures [26]. This is illustrated in Fig. 10 for the low-sulphur steel A. There is a good coincidence of the minimum in $K_{I,i}$ values derived from SRL tests in high-temperature water and the minimum in reduction of area, measured in tensile tests in air at similar strain rates. On the other hand, as shown in Fig. 9, the SICC growth rates subsequent to initiation were very similar for different materials for given temperatures and loading rates. DSA therefore seems to affect the initiation process itself (susceptibility, thresholds for onset and disappearance of EAC) rather than to directly influence the subsequent EAC growth (there is of course a strong indirect effect on crack growth, if initiation does not take place).

In EAC, DSA is especially important in dynamic crack-tip plasticity. DSA may result in an increase of yield/tensile strength, strain hardening exponent, creep rate, and finally in an increased crack-tip strain and strain rate. Microscopically, DSA results in an inhomogeneous localization of deformation, an increase of dislocation density, and planar deformation. These factors can result in a reduction of the local fracture toughness and also favour brittle crack extension or mechanical rupture of the protective oxide film and therefore crack advance by anodic dissolution/hydrogen embrittlement mechanisms. EAC in LAS has been observed under temperature/stain rate conditions or in materials, where no, or only minor DSA effects were present. DSA is therefore not a prerequisite for EAC and best regarded as an additional contribution to the EAC process.

The DSA response is governed by the concentration of free interstitial carbon and nitrogen, which strongly depend on the steel making or welding process, the thermal history or heat treatment (annealing- or post-weld heat treatment temperature) and on the chemical composition (C_{tot}, N_{tot}, Al, V, Ti, Cr, Mo, O, Mn, etc.) of the steel. Alloying elements, which have a strong affinity to C or N, such as Al, Cr, and Mo, which form nitrides or carbides, may result in a reduction of the residual concentration of free C and N. Differences in free C and N content of otherwise identical or similar LAS may be one important further reason for the relevant scatter of EAC CGR data and especially for the different trends observed in the temperature dependence of EAC.

Because of the different morphology of the MnS-inclusions in weld materials (small spherical inclusions) with respect to wrought steels (large, elongated inclusions), a higher EAC resistance was generally attributed to weld materials, which was not confirmed in this work. But weld metals often have a very low aluminum and high oxygen content. The very high affinity of oxygen to aluminum (formation of aluminum oxide inclusions) further reduces the beneficial effect of the aluminum concerning DSA. Therefore welds might be more susceptible to EAC in the DSA temperature–strain rate range than generally thought so far.

3.3.3. Microstructure

The effect of different microstructures was investigated in the loading rate range of maximum SICC susceptibility ($dCOD_{LL}/dt = 2–4·10^{-6}$ mm/s) in oxygenated high-temperature water with a DO/sulphate content of 8 ppm/65 ppb at a temperature of 288 and 250 °C. The base metal D, weld filler E and heat-affected zone (H) materials were from the circumferential weld between the lower and upper cylindrical shell of the German Biblis C PWR RPV, which was not commissioned. The base metal had a bainitic microstructure and the weld filler material revealed a fine-grained ferritic weld structure with finely dispersed and very small spherical MnS-inclusions. The crack plane in the HAZ was positioned in the peak hardness coarse grained zone close to the fusion line. A peak microhardness of 350 HV 0.5 was measured in this region.

At 250 °C, the SICC initiation stress intensity factors $K_{I,i}$ and SICC growth rates were comparable for all three microstructures (Fig. 9). At 288 °C (Fig. 14), the SICC growth rates were again comparable, but the HAZ material G and weld filler metal E revealed significantly lower and higher $K_{I,i}$ values than the corresponding base metal D. These increased and reduced SICC susceptibilities at 288 °C might be related to the higher yield strength of the HAZ G (similar MnS-morphology as base metal D) and the favourable

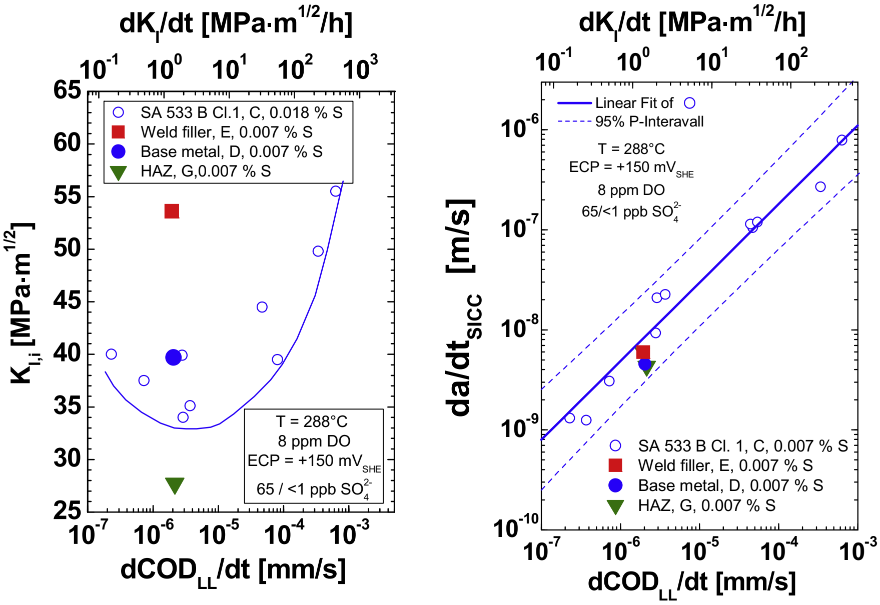

Fig. 14. Effect of microstructure on SICC initiation (left plot) and crack growth (right plot) at 288 °C.

MnS-morphology in the weld filler E (same sulphur content and similar DSA susceptibility and yield strength level as base metal).

3.3.4. Yield strength/hardness and heat treatment

Different yield strength/hardness levels in the high-sulphur steel C were produced by various heat treatments (Table 5), which did not affect the MnS-morphology. Besides the bainitic microstructure (Q+T), which is characteristic for the RPV base metal, a martensitic (Q) and a ferritic-pearlitic microstructure (N) were produced by austenizing/water quenching and austenizing/slow furnace cooling. The SICC behaviour of these microstructures in the loading range of maximum SICC susceptibility (dCOD$_{LL}$/dt = 2–4·10^{-6} mm/s) in oxygenated, high-temperature water with a DO/sulphate content of 8 ppm/65 ppb at 288 °C was then further compared to the weld metal E and the weld HAZ material G with different yield strength/hardness, but also different sulphur contents and DSA susceptibilities (whereas DSA effects are expected to be moderate at 288 °C).

The SICC initiation stress intensity factor $K_{I,i}$ of the normalized ferritic-pearlitic microstructure was slightly smaller than that of the simultaneously tested quenched and tempered bainitic microstructure of the same heat (Fig. 15), but the value was within the typical scatter range for this material and these specific conditions (see Fig. 5). The SICC growth rates were comparable for both microstructures (Fig. 15). Similar to the peak hardness HAZ G, the martensitic microstructure with an excessive hardness of 466 HV5 revealed an increased SICC susceptibility (lower $K_{I,i}$ values) over the standard base metal. The SICC growth rates of the non-annealed martensitic microstructure was significantly higher than in the other material conditions and in the stress-relieved HAZ G (Fig. 15). This eventually might indicate a different crack growth mechanism.

Fig. 16 shows the effect of Vickers hardness on the SICC growth rates for these three heat treatment conditions of material C as well as for the weld filler E and HAZ G in oxygenated high-temperature water with a DO/sulphate content of 8 ppm/65 ppb at 288 °C and at a loading rate dCOD$_{LL}$/dt of 2–4·10^{-6} mm/s. Up to a critical hardness of approximately 350 HV5 (or a critical yield strength level of about 800 MPa), the SICC growth rates were very similar for all material conditions and did not depend on the hardness or yield strength level. Above this threshold significantly higher SICC rates were observed. This threshold correlates well with corresponding thresholds of 300–400 HV5 for the occurrence of hydrogen-induced [22] or interganular [21] SCC in C & LAS in high-temperature water.

It is stressed that a martensitic microstructure does not occur in properly fabricated C & LAS pressure boundary components. The hardness of weld HAZ is controlled and limited to values <350 HV5 by quality assurance measures/careful selection of welding parameters/post weld heat treatment. The degree of cold work (bending), which can be accepted without any heat treatment is also strictly limited.

3.4. Quantitative description of SICC crack growth

In SRL tests at PSI under highly oxidizing BWR/NWC conditions (ECP ⩾ +50 mV$_{SHE}$, DO ⩾0.4 ppm) above a K_I value of 25 MPa m$^{1/2}$ the SICC CGRs in the loading rate range of 0.05–500 MPa m$^{1/2}$/h increased with increasing loading rate dK_I/dt according to a power law relationship with an exponent of 0.8 (see Figs. 5 and 7), but as a first approximation the rates were not dependent on the actual K_I values up to 60 MPa m$^{1/2}$. High SICC growth rates between 10^{-9} and 9·10^{-7} m/s (0.1–70 mm/day) were observed under SRL and

Table 5
Applied heat treatments and resulting properties of the RPV steel C

Parameter	*Q* + *T*	*N*	*Q*
Heat treatment	915 °C/12 h/Air/860 °C/12 h/WQ 660 °C/12 h/FC/610 °C/40 h/FC 550 °C/12 h/FC/550 °C/12 h/FC	900 °C/30 min/FC	900 °C/30 min/WQ
Microstructure	Bainitic	Ferritic-pearlitic	Martensitic
Vickers hardness	197 HV10	260 HV10	466 HV10
$R_p^{288\ ^\circ C}$	411 MPa	577 MPa	960 MPa

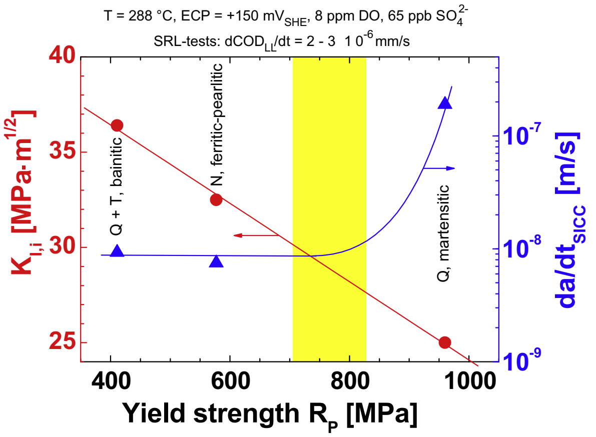

Fig. 15. Effect of yield strength on SICC susceptibility and crack growth in high-sulphur steel C.

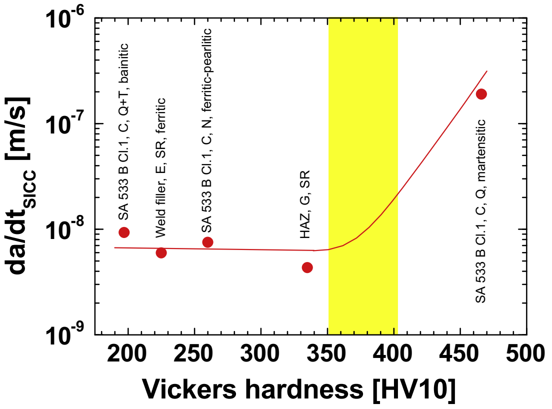

Fig. 16. Effect of hardness on SICC crack growth rate at 288 °C.

highly oxidizing BWR/NWC conditions. Under these conditions maximum SICC CGRs in LAS with a hardness of <350 HV5 can be described as follows:

$$da/dt_{SICC} = 6 \cdot 10^{-9} \cdot (dK_I/dt)^{0.8} \quad \text{in m/s and MPa m}^{1/2}\text{/h} \qquad (1)$$

for $25\ \text{MPa m}^{1/2} \leqslant K_I \leqslant 60\ \text{MPa m}^{1/2}$, $0.05\ \text{MPa m}^{1/2}\text{/h} \leqslant dK_I/dt \leqslant 500\ \text{MPa m}^{1/2}\text{/h}$ and ECP $\geqslant +50\ \text{mV}_{SHE}$, $250\ °\text{C} \leqslant T \leqslant 288\ °\text{C}$.

3.5. Comparison to SSR test results

The effects of strain rate [7,15], temperature [7,12,13], ECP [7–13], sulphate [12,13] or steel sulphur content [12,13,15] on SICC initiation and growth in SSR experiments with smooth tensile specimens are in good qualitative agreement with the observations in SRL tests on pre-cracked fracture mechanics specimens. In general, the steel sulphur content often had a more pronounced effect in SSR experiments with smooth specimens, where SICC cracks usually initiated from MnS-inclusions, which intersected the water-wetted steel surface. With respect to smooth specimens, a high-sulphur crack-tip electrolyte in pre-cracked specimens is facilitated by the large number of dissolvable MnS-inclusions, which are intersected by the crack flanks, and the ease of enrichment of the resulting sulphides by the restricted mass transport in the high-aspect ratio crack crevice geometry, in particular by migration in case of high ECPs and high DO contents in the bulk environment.

4. Comparison of SRL and very low and low-frequency fatigue test results

Very low-frequency corrosion fatigue (vLFCF) constant load amplitude tests with asymmetric saw tooth loading at a low and high load ratio of 0.2 ($\Delta K = 51.1$–64.4 MPa m$^{1/2}$, $\Delta t_R = 94$ h) and 0.8 ($\Delta K = 11$–13 MPa m$^{1/2}$, $\Delta t_R = 27.8$ h) were performed in water at 288 °C with a DO of 8 ppm and 60 or 65 ppb SO_4^{2-}.

In vLFCF tests with a low load ratio R of 0.2 and an extremely long rise time of 94 h, SICC crack growth could be resolved by DCPD during each individual fatigue cycle (Fig. 17). The crack growth initiation stress intensity factor $K_{I,i}$ and the true SICC growth rates da/dt_{SICC} in each fatigue cycle are shown for the high-sulphur alloy C and the low-sulphur material A in Fig. 18. SICC occurred only during the last part of the rising load phase of the fatigue cycles. Because of the small crack increment per fatigue cycle, details of crack growth during individual fatigue cycles could be not resolved in case of the tests with the high load ratio and small ΔK, and therefore only a mean SICC crack growth rate $\langle da/dt_{SICC} \rangle$ over many cycles could be given. Here, as in normal CF tests, an apparent time-based crack growth rate $da/dN/\Delta t_R$ is usually calculated.

In the high-sulphur alloy C, SICC initiation was observed by DCPD already during the first fatigue cycle (Figs. 17 and 18). The observed $K_{I,i}$ value and SICC growth rate were thereby comparable to the results of the corresponding SRL tests with the same loading rate (Figs. 5 and 19). In the next two cycles $K_{I,i}$ values increased but stabilized after the third cycle, probably because of (surface roughness and oxide film induced) crack closure effects. The SICC growth rates remained approximately constant during all the fatigue cycles (Fig. 18).

In the low-sulphur alloy A, SICC initiation was first observed by DCPD during the second cycle (Fig. 18). In the next cycle, the $K_{I,i}$ value decreased; the SICC growth rates increased and then stabilized after the third cycle (Fig. 18). The somewhat different behaviour during the stabilization phase is probably caused by localized crack growth in alloy A during the first fatigue cycles, since less crack initiation sites were activated in the initial rising load phase in this material. After stabilization, the $K_{I,i}$ values and SICC CGRs were comparable for both alloys (Fig. 18).

After stabilization, SICC occurred only during the last 20–25% of the rising load phase of the fatigue cycles, i.e. at an effective load ratio $R_{eff} = K_{I,i}/K_{I,max}$ of ≈0.8. Since SICC growth only occurred during a small part of the whole rising load phase, the apparent SICC CGR $da/dN/\Delta t_R$ may be significantly lower than the real SICC rates da/dt_{SICC} during each cycle. In Fig. 19(a), the true SICC growth rates

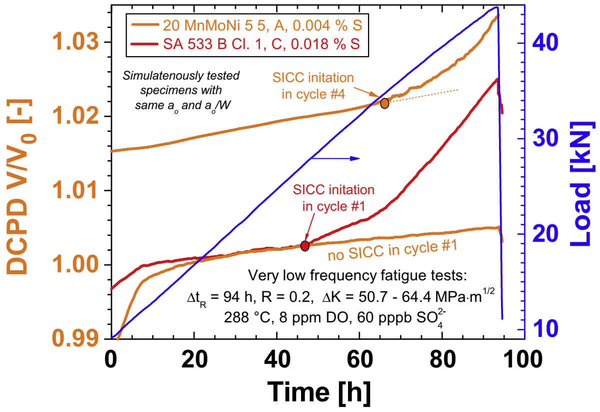

Fig. 17. DCPD signal at selected cycles in very low frequency fatigue tests with the low- and high-sulphur steel A and C at 288 °C.

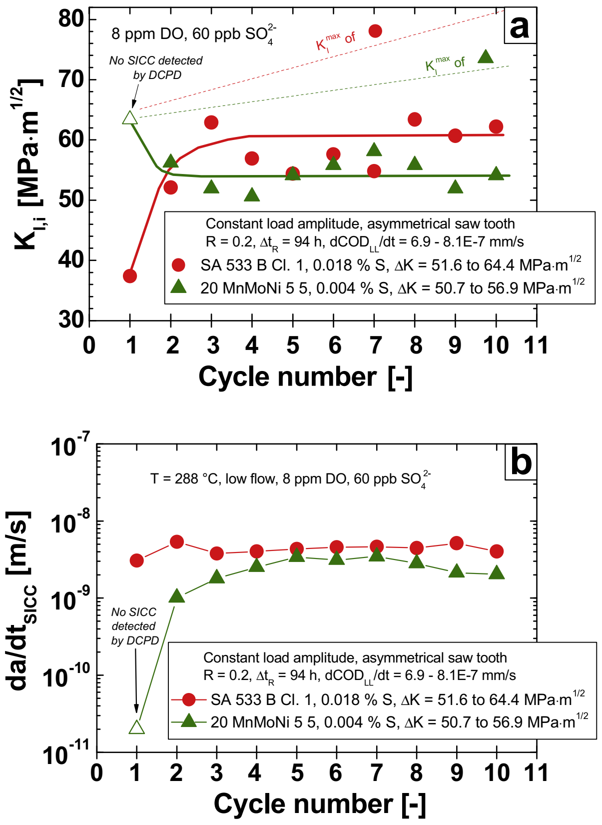

Fig. 18. (a) Crack growth initiation stress intensity factor $K_{I,i}$ in each fatigue cycle in very low-frequency fatigue tests with the low- and high-sulphur steels A and C. (b) Corresponding true SICC growth rates in each fatigue cycle.

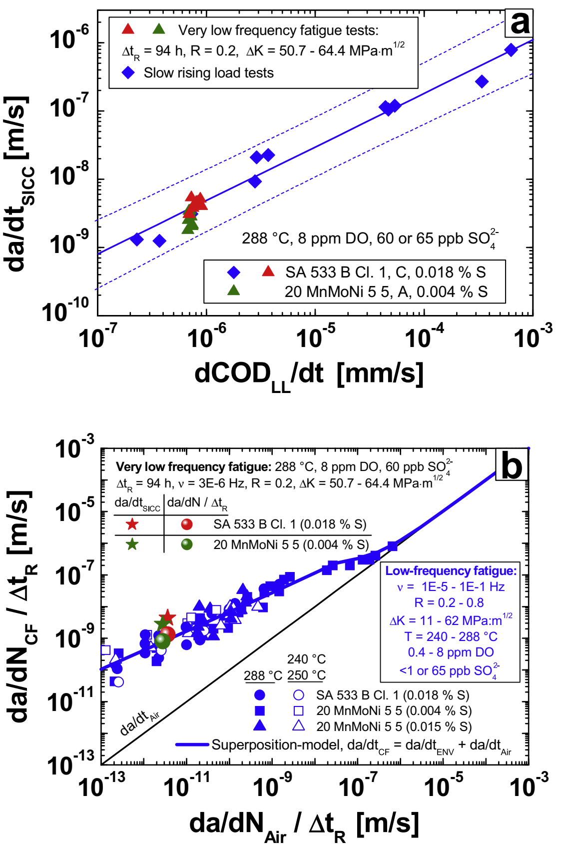

Fig. 19. (a) Comparison of true SICC growth rates in vLFCF tests with corresponding rates in SRL experiments. (b) Comparison of true and apparent SICC growth rates in very low-frequency fatigue experiments with normal low-frequency corrosion fatigue growth rates in time–domain plot.

from vLFCF tests are compared to SICC results from SRL tests under identical environmental conditions. Within the typical scatter range, these true SICC growth rates were identical to those of SRL experiments for comparable loading rates.

In Fig. 19(b), the true and apparent SICC rates da/dt_{SICC} and $da/dN/\Delta t_R$ of the vLFCF experiments are compared with normal LFCF test results of PSI in the frequency range from 10^{-5} to 10^{-1} Hz in a so-called time–domain plot. Here the apparent SICC and CF rates in high-temperature water are plotted versus the corresponding apparent fatigue growth rates in air [27] under otherwise identical conditions. The true da/dt_{SICC} were in the upper bound region of experimental results, whereas the apparent rates were in the middle on the data on the BWR/NWC regression curve for a wide range of loading and material conditions. This thus demonstrates that SICC and CF are closely related phenomena.

The vLFCF results clearly demonstrate, that monotonic SRL test results at a high ECP with only minor, local SICC should not be interpreted as definite evidence of a low SICC cracking susceptibility. These crack initiation problems can be easily overcome by suitable repeated loading. Furthermore, CF tests have shown, that CF or SICC may occur at much lower K_I^{max} values than in the SRL experiments with long incipient crack [20] and this is also confirmed by service cracking incidents [1–7]. The high $K_{I,i}$ values of the SRL experiments should therefore not be misinterpreted as SICC threshold $K_{I,SICC}$.

5. Control factors and conjoint requirement for SICC

As discussed in Section 3.1, the occurrence of SICC might be related to a critical sulphur anion threshold in the crack-tip electrolyte (Figs. 7a and 7b). As shown in Fig. 20, in oxygenated high-temperature water (simulated BWR/NWC environment) a fundamental relationship between the EAC CGR and the crack mouth opening displacement rate $dCOD/dt_{LL}$ (which, as first approximation, might be regarded as a rough measure for crack-tip strain rate) seems to exist over a wide range of loading conditions covering SRL, cyclic fatigue and constant load tests. The observed behaviour thus suggests a fundamental relationship between EAC CGR and crack-tip strain rate and further confirms that SCC [26], SICC and CF [20] are related phenomena, which are governed by the same basic processes or mechanisms.

Both, the experimental parameter effects in this work (e.g., Figs. 7 and 20) and other PSI investigations [20,26] as well as the Ford & Andresen EAC crack growth model [4,25] indicate that the SICC growth from incipient long cracks is essentially governed by the crack-tip strain rate and the activity of sulphur-anions (affecting repassivation/pH/oxide film stability) in the crack-tip electrolyte. The onset and extent of SICC is crucially dependent on simultaneously maintaining a slow, positive crack-tip strain rate and a critical sulphur anion concentration in the crack-tip electrolyte. If these two conjoint requirements are not met, no SICC or only minor environmental acceleration of fatigue crack growth are observed in SRL or low-frequency fatigue tests, respectively. If the critical sulphur threshold concentration is exceeded, the SICC CGR depends primarily on the crack-tip strain rate and increases with increasing strain rate up to an upper critical limit, where environmental effects disappear and pure mechanical fatigue dominates.

These two local factors are governed by a system of interrelated and synergistic corrosion system parameters: In general,

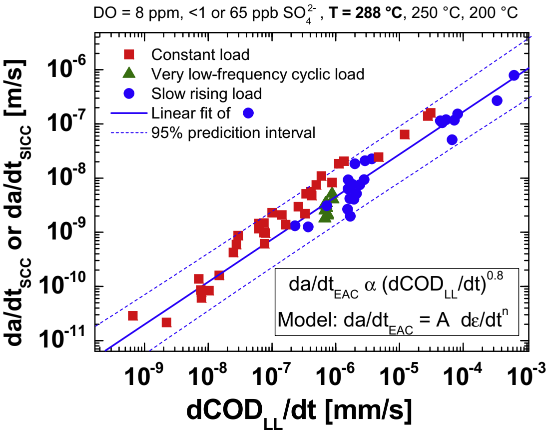

Fig. 20. Correlation between EAC CGR and crack mouth opening displacement rate over a very wide range of different loading conditions for materials C (all loading conditions) as well as A and B (constant load only).

the crack-tip strain rate increases with increasing loading rate/loading frequency (as well as load level), crack growth rate, yield strength and DSA susceptibility. The sulphur anion content in the crack-tip environment increases with increasing steel sulphur content, concentration of sulphur-anions in the bulk environment outside the crack, crack growth rate (exposure of new fresh dissolvable MnS-inclusions by the growing crack) and corrosion potential/DO content (anion enrichment in the crack enclave by migration). The threshold conditions for SICC are directly related to crack-tip chemistry and crack-tip strain rate/crack growth rate, rather than to loading parameters or bulk environment conditions per se e.g., suitable combinations of different system parameters may help to exceed the critical crack-tip sulphur-anion concentration, provided that there is at least one source of sulphur (MnS-inclusions or sulphur anion in the bulk environment).

6. Comparison to SICC incidents and service experience

The operating experience (Section 1.1) fits well to the accumulated experimental/mechanistic background knowledge on EAC behaviour in the system C & LAS-high-temperature water. Both show the same qualitative parameter trends, e.g., for oxygen, flow rate, or strain and strain rate. Both confirm the high SCC resistance of LAS under steady-state power operation and static loading conditions and clearly reveal that slow, positive (tensile) straining with associated plastic yielding and sufficiently oxidizing conditions are essential for SICC initiation in high-purity high-temperature water. Since primary design stresses are generally limited to values below the elastic limit, thermal-hydraulics (e.g., thermal stratification) and local stress raisers therefore played a key role for SICC/CF in the field and were generally more important than material or water chemistry aspects.

By taking the exact boundary conditions in lab tests and in the field into account, no major discrepancy between operating experience and trends in laboratory data could be found. The SICC cracking incidents can be readily rationalized by the SICC susceptibility conditions identified in Section 1.2 [1,4,7]. The apparently higher cracking frequency in lab tests may be easily explained by the beneficial effect of a turbulent flow rate in the field (which is characteristic for most component locations) for SICC initiation and the conjoint threshold conditions for the onset of SICC or CF with regard to ECP (or DO content), strain rate, strain and temperature. In general, for many transients/component locations, one or several threshold conditions are not satisfied. Even if all requirements would be fulfilled, the SICC/CF initiation process may consume a long incubation period/large number of fatigue cycles in the absence of pre-existing defects or cracks, in particular for small strains, and therefore, extend over a significant part (or even the whole part) of the plant lifetime. The SRL experiments in this work started with a sharp fatigue pre-crack that is ‘ready’ to propagate. Similarly, SSR tests with smooth specimens normally involve high applied plastic strains and plastic yielding of the un-cracked ligaments. Both cases are thus significantly different from, and much more severe than the situation in most components [1].

Very high SICC growth rates of 0.1–70 mm/day were observed in SRL tests in simulated BWR/NWC environment under linear-elastic loading conditions with slow positive dK_I/dt at K_I values >25 MPa m$^{1/2}$. Even though such high rates represent extreme situations or limiting cases, they may help to understand several SICC cracking incidents and to explain why relatively few loading transients had sometimes produced deep cracks. A common feature of most SICC cracking incident analyses has been clear fractographical evidence for the damage having been accumulated intermittently, with several, distinct phases of crack propagation during plant transients with relevant dynamic straining (e.g., arising from thermal stratification, thermal and pressurization cycles, etc.), which were interrupted by long periods of stationary BWR operation without crack growth.

Service experience, on the other hand, has shown that SICC cracks can initiate and grow from notches (with surface plasticity) at significantly lower stress levels than it might be expected based on the relatively high $K_{I,i}$ values for SICC initiation for deep and fully constraint incipient cracks in SRL experiments without repeated loading.

7. Summary and conclusions

The SICC behaviour of different LAS RPV and piping steels and of a RPV weld filler/weld HAZ material was characterized under simulated BWR/NWC conditions by SRL and very low-frequency fatigue tests with pre-cracked fracture mechanics specimens.

Under highly oxidizing BWR/NWC conditions (ECP $\geqslant$+50 mV_{SHE}, $\geqslant$0.4 ppm dissolved oxygen), the SICC crack growth rates were comparable for all materials (hardness <350 HV5) and increased (once initiated) with increasing strain/loading rates and with increasing temperature with a possible maximum/plateau at 250 °C. A high minimum K_I value of 25 MPa m$^{1/2}$ had to be exceeded to initiate SICC in SRL tests, which should not be regarded as SICC threshold. Above this value, the SICC rates increased with increasing loading rate dK_I/dt according to a power law relationship with an exponent of 0.8, but as a first approximation the rates were not dependent on the actual K_I values up to 60 MPa m$^{1/2}$. High SICC growth rates of 0.1–70 mm/day were observed under these conditions in the loading rate range dK_I/dt of 0.05–500 MPa m$^{1/2}$/h.

A maximum of SICC initiation susceptibility occurred at intermediate temperatures around 200–250 °C and at slow strain/loading rates in all materials. In contrast to crack growth, the SICC initiation susceptibility was affected by environmental and material parameters within certain limits.

The experimental observations suggest that SICC from incipient cracks is essentially governed by the crack-tip strain rate and the concentration of sulphur-anions in the crack-tip electrolyte. The onset and extent of SICC is crucially dependent on simultaneously maintaining a slow, positive crack-tip strain rate below an upper threshold and a critical sulphur anion content in the crack-tip electrolyte. If these two conjoint requirements are not met, no SICC or only minor environmental acceleration of fatigue crack growth are observed in SRL and low-frequency fatigue tests, respectively.

In case of mechanical loading in the critical load rate and load level range, suitable combinations of material and environmental parameters may help to simultaneously exceed the critical crack-tip sulphur anion concentration, provided that there is at least one source of sulphur (MnS-inclusions or sulphur anion in the bulk environment).

Acknowledgements

The data of this paper have been generated within the SpRK, RI-KORR and the CASTOC projects. The financial support for these projects by the Swiss Federal Nuclear Safety Inspectorate (HSK), the Swiss Federal Office of Energy (BFE), Swissnuclear and the Swiss Federal Office for Education and Science (BBW) is gratefully acknowledged. Thanks are also expressed to U. Ineichen, U. Tschanz, B. Gerodetti, and E. Groth (all PSI) for their experimental contribution to this work.

References

[1] H.P. Seifert, S.Ritter, Research and service experience with environmentally-assisted cracking of carbon and low-alloy steels in high-temperature water, SKI-Report 2005:60, Stockholm, Sweden, 2006. <www.ski.se>.
[2] H.P. Seifert, S. Ritter, J. Hickling, Power Plant Chem. 6 (2004) 111.
[3] P. Scott, D. Tice, Nucl. Eng. Des. 119 (1990) 399.
[4] J. Hickling, D. Blind, Nucl. Eng. Des. 91 (1986) 305.
[5] F.P. Ford, Environmentally-assisted cracking of low-alloy steels, EPRI NP-7473-L, Electric Power Research Institute, January 1992.
[6] Y.S. Garud et al., Corrosion fatigue of water-touched pressure retaining components in power plants, EPRI TR-106696, Final Report, November 1997.
[7] E. Lenz, N. Wieling, Nucl. Eng. Des. 9 (1986) 331.
[8] T. Arai, M. Mayuzumi, Effect of dissolved oxygen concentration and material factors on stress corrosion cracking of low-alloy Steels, NACE Corrosion 97, Paper 90, NACE, USA, 1997, p. 90-1.
[9] J. Congleton, T. Shoji, R.N. Parkins, Corros. Sci. 25 (1985) 633.
[10] M.E. Indig et al., Rev. Coat. Corros. 5 (1982) 173.
[11] T. Shoji, in: Proceedings of the 3rd International Atomic Energy Agency Specialist's Meeting on Sub-critical Crack Growth, Technical Sessions II, II and IV, Vol. 2, NUREG/CP-0112, ANL-90/22, Moscow, USSR, 1990, p. 109.
[12] T. Shoji, H. Takahasi, S. Aizawa, M. Saito, in: Proceedings of the 3rd International Symposium on Environmental Degradation of Materials in Nuclear Power Systems – Water Reactors, 1988, p. 251.
[13] G. Sund, in: Proceedings of the 3rd International Atomic Energy Agency Specialist's Meeting on Subcritical Crack Growth, Technical Sessions II, II and IV, Vol. 2, NUREG/CP-0112, ANL-90/22, Moscow, USSR, 1990, p. 3.
[14] H. Gladen, H. Kaesche, Nucl. Eng. Des. 151 (1994) 463.
[15] H. Friedrich, J. Frank, H. Gladen, M. Stratmann, Stress corrosion cracking of low-alloy steels under high pressure and high-temperature conditions, Corrosion 96, Baltimore, MD, USA, Paper 98, 1996, p. 98-1.
[16] O.K. Chopra, W.J. Shack, Nucl. Eng. Des. 184 (1998) 49.
[17] G. Nakao, M. Higuchi, H. Kanasaji, K. Iida, Y. Asasa, in: W.A. Van der Sluys, R.S. Piascik, R. Zawierucha, (Eds.), Effects of the Environments on the Initiation of Crack Growth, ASTM STP 1298, ASTM, 1997, p. 232.
[18] O.K. Chopra, W.J. Shack, Effect of LWR coolant environments on the fatigue life of reactor materials – final report, NUREG/CR-6909, ANL-06/08. US NRC, Washington, DC, USA, February 2007.
[19] W.A. Van Der Sluys, in: Proceedings of the 6th International Symposium on Environmental Degradation of Materials in Nuclear Power Systems – Water Reactors, NACE/TMS/ANS, San Diego, California, USA, August 1–5 1993, p. 1.
[20] H.P. Seifert, S. Ritter, Corros. Sci. 50 (2008) 1884.
[21] M. Tsubota et al., in: 6th International Conference on Environmental Degradation of Materials in Nuclear Power Systems – Water Reactors, San Diego, CA, USA, August 1–5, 1993, p. 53.
[22] J. Hickling, Wasserstoffinduzierte Spannungsrisskorrosion in niedriglegierten Stählen, 4th MPA-Seminar, Paper No. 7, Stuttgart, Germany, October 4–5 1978.
[23] P.M. Yukawich, C.W. Hughes, Pract. Metallogr. 20 (1997) 1.
[24] M.O. Speidel, R.M. Magdowski, Int. J. Pres. Ves. Pip. 34 (1988) 119.
[25] F.P. Ford, P.L. Andresen, in: W. Cullen, (Ed.), 3rd International IAEA Specialist's Meeting on Subcritical Crack Growth, vol. 1, NUREG/CP-0112, Moscow, USSR, May 14 – 17, 1990, p. 105.
[26] H.P. Seifert, S. Ritter, J. Nucl. Mater. 372 (2008) 114.
[27] E. Eason et al., Nucl. Eng. Des. 184 (1998) 89.